

MOST: MR reconstruction Optimization for multiple downStream Tasks via continual learning

Hwihun Jeong, Se Young Chun, Member, IEEE, and Jongho Lee, Member, IEEE

Abstract— Deep learning-based Magnetic Resonance (MR) reconstruction methods have focused on generating high-quality images but they often overlook the impact on downstream tasks (e.g., segmentation) that utilize the reconstructed images. Cascading separately trained reconstruction network and downstream task network has been shown to introduce performance degradation due to error propagation and domain gaps between training datasets. To mitigate this issue, downstream task-oriented reconstruction optimization has been proposed for a single downstream task. Expanding this optimization to multi-task scenarios is not straightforward. In this work, we extended this optimization to sequentially introduced multiple downstream tasks and demonstrated that a single MR reconstruction network can be optimized for multiple downstream tasks by deploying continual learning (MOST). MOST integrated techniques from replay-based continual learning and image-guided loss to overcome catastrophic forgetting. Comparative experiments demonstrated that MOST outperformed a reconstruction network without finetuning, a reconstruction network with naïve finetuning, and conventional continual learning methods. This advancement empowers the application of a single MR reconstruction network for multiple downstream tasks. The source code is available at: <https://github.com/SNU-LIST/MOST>

Index Terms—Continual learning, MRI reconstruction, Downstream tasks, Multi-task

I. INTRODUCTION

MAGNETIC Resonance Imaging (MRI) has gained considerable prominence in clinical practice due to its inherent advantages including soft tissue sensitivity, non-invasiveness, and no radiation exposure. The advent of deep learning-based techniques has ushered in a new era of innovation in MRI such as disease classification [1-4], tumors or lesions segmentation [5, 6], acquisition [7], and image processing [8, 9]. In particular, the scan time reduction has been a target of innovation and various reconstruction neural networks have been proposed, yielding high-quality images even from highly undersampled k-space data [10-12]. When evaluating reconstructed images, the gold-standard is the assessment by radiologists, which is often impractical due to high expense. Consequently, many studies rely on quantitative

metrics such as the Structural Similarity Index (SSIM) and Peak Signal-to-Noise Ratio (PSNR) [12, 13]. Despite the utility, such metrics have limitations in reflecting the evaluation of radiologists. More importantly, when the reconstruction network is connected to a downstream task network (e.g., segmentation network), optimizing these metrics in the reconstruction network has been shown to deliver suboptimal outcomes in the downstream task [14, 15]. As a result, efforts have been made to design a “downstream-oriented” reconstruction network, optimizing it based on the performance of downstream tasks [16-19]. So far, however, these methods are designed for a single downstream task (Fig. 1a). Hence, when multiple downstream tasks exist, the current solution is to develop multiple reconstruction networks each of which is optimized for individual tasks, which may not be practical.

In this study, we propose an approach that one can optimize a reconstruction network for multiple downstream tasks. Simple expansion from single-task to multi-task optimization is not straightforward [20]. Therefore, we consider a realistic scenario where the reconstruction network is sequentially finetuned for pretrained downstream task networks, assuming limited access to the training dataset of ready-trained tasks. (Fig. 1b) This sequential finetuning strategy reduces the computational burden of processing the entire dataset for all previous tasks and handles real-world environments where multiple downstream tasks are progressively developed and introduced.

When sequentially training a reconstruction network for multiple downstream tasks, one may consider naïve finetuning for the current task. This approach, however, can lead to a well-known issue of catastrophic forgetting, where performance on previously optimized tasks degrades substantially [21-25]. To overcome this issue and sustain the performances for the multiple downstream tasks, we propose to embrace the notion of continual learning [26, 27] and tailor it to our approach. Our contributions are summarized as follows:

1. We enable an MR reconstruction network to be sequentially finetuned for multiple downstream tasks.

This work is supported by the National Research Foundation of Korea grant funded by the Korea government (No. NRF-2022R1A4A1030579), Korea Agency for Infrastructure Technology Advancement grant funded by the Ministry of Land, Infrastructure and Transport (Grant 21NPSS-C163415-01), Samsung Electronics Co., Ltd (I0201216-08215-01), INMC, SEPRI and IOER at Seoul National University.

H. Jeong, SY. Chun, and J. Lee are with the Department of Electrical and Computer Engineering, Seoul National University, Seoul 08826, Republic of Korea. (e-mail: hwihuni@snu.ac.kr; sychun@snu.ac.kr; jonghoyi@snu.ac.kr)

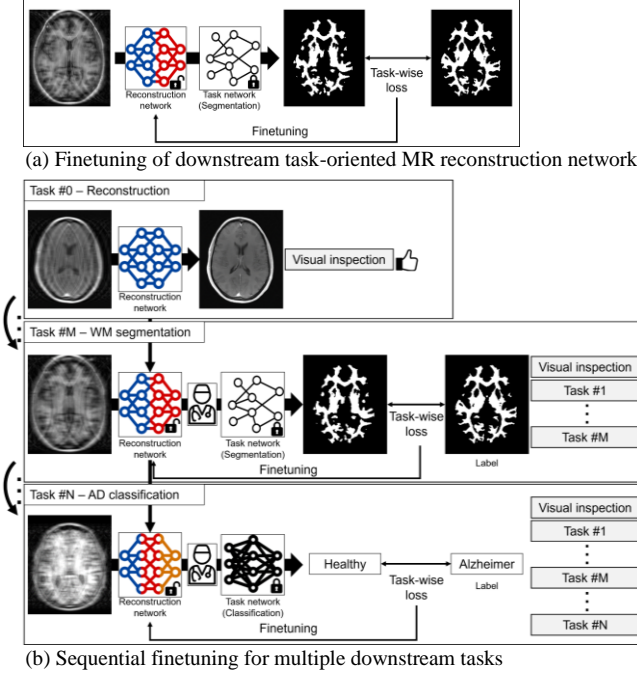


Fig. 1. (a) Combining individually trained reconstruction and downstream networks may result in performance degradation, stemming from error propagation or domain gap issues. Task-oriented finetuning can mitigate these challenges. (b) In scenarios with progressively developed downstream tasks, sequential finetuning of the reconstruction network can be an effective solution. However, naïve finetuning can lead to catastrophic forgetting, underscoring the importance of continual learning.

2. Replay-based continual learning method is adopted to prevent catastrophic forgetting.
3. Image-guided loss is incorporated to give richer information in mitigating catastrophic forgetting.

II. RELATED WORKS

A. MR reconstruction

With the advent of deep learning-based image processing, the deep neural network has emerged as a powerful tool for MR reconstruction [28]. Initially, end-to-end supervised networks were employed, taking undersampled k-space data (or aliased image) as input and generating fully sampled k-space data (or aliasing-free image) [29-31]. Then, model-based frameworks were developed, which enforce the forward model of k-space undersampling. These methods typically incorporate an unrolled network structure [10, 11], which alternates between neural network and data consistency, resulting in robust and high-quality reconstruction for various undersampling factors and image contrasts.

B. Clinical evaluation of MRI images

Computer vision techniques such as classification and segmentation have been successfully adopted for the clinical evaluation of MRI images [32]. Classification techniques are used for diagnosing diseases such as Alzheimer's disease [33], Parkinson's disease [4], Schizophrenia [34], and brain tumor [35]. In the case of segmentation, a lesion segmentation

network is used for localizing the region of the brain associated with brain tumor [6], ischemia [5], or multiple sclerosis [36]. Segmentation is also applied to segment sub-structures of the brain [37, 38].

C. Continual learning

Continual learning enables a neural network to learn from new data over time without forgetting previously learned information, hence, preventing catastrophic forgetting. Continual learning algorithms aim to address this challenge by enabling a network to retain previously acquired knowledge while adapting to new data. A popular approach is a replay-based algorithm, which stores subsets of past task data and utilizes them during the training process of the current task. In MRI, the deployment of continual learning has recently been suggested only in a few segmentation studies. One example is the sequential training of a segmentation network for cardiac segmentation over scanner types [39]. A similar strategy of sequential training over scanner type was adopted for the segmentation of brain tissues [40]. Another application was sequential training of a segmentation network starting with normal brain structures and subsequently on the white matter lesions [41].

III. METHODS

A. Finetuning of downstream task-oriented MR reconstruction network

Accelerated MRI reconstruction aims to produce high-quality images from undersampled k-space data, making them comparable to fully sampled data. Traditionally, an MR reconstruction model denoted as f_R with parameter θ , is trained using the fidelity loss function \mathcal{L}_R such as SSIM loss where x represents an aliased image, and y represents an aliasing-free label image:

$$\theta^* = \underset{\theta}{\operatorname{argmin}} \mathcal{L}_R(f_R(x; \theta), y). \quad (1)$$

However, when this reconstructed network is used for a downstream task such as segmentation and classification, a simple cascade of independently trained reconstruction network and downstream network might not be optimal. For example, the reconstructed images may have different characteristics from the images trained for the downstream network due to the imperfection of the reconstruction network or domain gaps between the two training datasets. To address this issue, finetuning of the reconstruction network with end-to-end data (cf., data pairs of aliased image and downstream task label) using a corresponding loss function is a valuable approach (Fig. 1a) [16-19]. This task-oriented reconstruction optimization can be written as follows:

$$\theta_{task}^* = \underset{\theta}{\operatorname{argmin}} \mathcal{L}(f_d(f_R(x; \theta)), z), \quad (2)$$

where f_d is the downstream task network, \mathcal{L} is the corresponding loss function (e.g., cross-entropy for

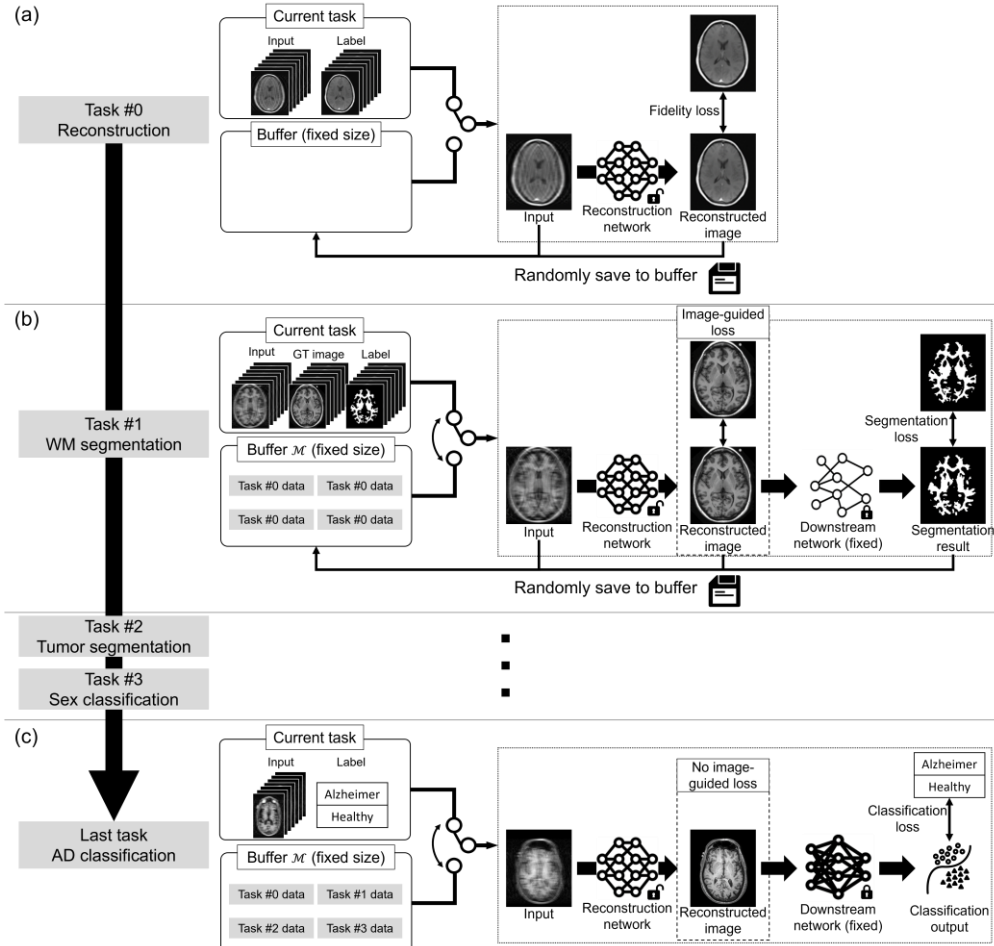


Fig. 2. Our MOST addresses the issue of catastrophic forgetting during multi-task finetuning. As finetuning advances, a fixed-size buffer stores input-output pairs, with newly added pairs replacing some of the old ones. Subsequent finetuning stages leverage this buffer data to mitigate catastrophic forgetting. Moreover, the image guided loss is introduced when finetuning for the segmentation task.

classification or DICE loss for segmentation), and z is the label (e.g., classification label or segmentation map).

B. Sequential finetuning for multiple downstream tasks

When multiple downstream tasks exist, the task-oriented optimization for multiple downstream tasks ($t = 1, 2, 3, \dots, T$) can be rewritten as follows:

$$\theta_{multi-task}^* = \underset{\theta}{\operatorname{argmin}} \sum_t \mathcal{L}_{dt}(f_{dt}(f_R(x_t; \theta)), z_t), \quad (3)$$

where \mathcal{L}_{dt} is the loss function of t -th downstream tasks, f_{dt} is the downstream task network. The end-to-end dataset of finetuning for t -th downstream task $D_t = \{x_t^i, z_t^i\}_{i=1}^{n_t}$ includes an aliased image x and a downstream task label z with the size of n_t . However, such multi-task learning is difficult to be optimized [20] and does not adapt well to real-world applications. In this work, we propose to apply continual learning for a single reconstruction network such that it can be sequentially finetuned for multiple downstream tasks (Fig. 1b). Our scenario assumes limited access to ready-trained datasets due to privacy concerns and computational costs. Initially, the reconstruction network f_R is trained exclusively for image

reconstruction using a loss function (\mathcal{L}_R) and a reconstruction dataset (D_R) as written in (1). Then, we sequentially finetune the reconstruction network for multiple downstream tasks:

$$\theta_t^* = \underset{\theta}{\operatorname{argmin}} \mathcal{L}_{dt}(f_{dt}(f_R(x_t; \theta)), z_t). \quad (4)$$

It is important to stress that the finetuning process exclusively targets the reconstruction network while downstream networks are fixed. When finetuning for the t -th downstream task, we assume that access to the full dataset of the previous downstream task ($D_p, p < t$) is restricted and only a small subset of the dataset is available.

C. Reconstruction network structure

For the reconstruction network, the end-to-end variational network, which is modified to work for a single coil setting [10, 12], is deployed (see Appendix).

D. MOST

In our proposed approach, MOST, replay-based continual learning is combined with an image-guided loss to prevent catastrophic forgetting during sequential finetuning for multiple downstream tasks (Fig. 2).

TABLE I
DETAILED INFORMATION REGARDING THE DATASET COMPOSITION IS ILLUSTRATED

Task	Reconstruction	WM segmentation	Tumor segmentation	Sex classification	AD classification
Dataset	FastMRI	OASIS 1	BraTS	IXI	ADNI
Input matrix size	320 × 320	176 × 208	240 × 240	150 × 200	176 × 176
Downstream task train/val	-	16165/1891 (slices)	48190/5734 (slices)	366/0 (subjects)	523/0 (subjects)
Finetuning train/val	22234/2116 (slices)	2440/305 (slices)	7259/915 (slices)	61/35 (subjects)	84/49 (subjects)
Test	5628 (slices)	5795 (slices)	14213 (slices)	105 (subjects)	185 (subjects)

For the replay, a fixed-size buffer denoted as \mathcal{M} is maintained to store a subset of input-output pairs from previous tasks. After finishing each task, we randomly select input-output pairs from that task and add them to the buffer (Fig 2). The buffer size remains constant throughout the finetuning process, with newly added data pairs replacing older ones. Hence, the number of data in the buffer is kept the same across the tasks.

Unlike conventional replay-based continual learning methods [26, 27, 42, 43], which generally combine the data of the current and previous tasks in the same mini-batch, our method presents a unique challenge in forming a combined mini-batch because the input data structure and label type can be different among tasks (e.g., segmentation: 2D input and 2D label vs. classification: 3D input and binary label). To address this challenge, data from the past task in the buffer is used in every K iteration (See Algorithm 1) during the finetuning process (Fig. 2b and 2c). The stored data are used in a round-robin fashion across the tasks.

In downstream tasks that generate images (e.g., segmentation tasks), we introduce an image-guided loss, \mathcal{L}_{IG} , to further enhance the finetuning process (Fig. 2b). This loss, which is calculated using a reconstruction loss \mathcal{L}_R , compute the difference between the intermediate reconstructed image $f_R(x_t; \theta)$ and the aliasing-free image y_t to enhance the

Algorithm 1 MOST framework

```

Initialize: datasets  $D$ , reconstruction network  $f_R$ ,  

downstream task networks  $f_{dt}$ , reconstruction loss  

function  $\mathcal{L}_R$ , downstream task loss functions  $\mathcal{L}_{dt}$ , learning  

rate  $\lambda$ 
1:  $\mathcal{M} \leftarrow \{\}$ 
2: for  $D_t$  in  $D$  do
3:   for  $k, x_t, y_t, z_t$  in enumerate( $D_t$ ) do
4:     if exist( $y_t$ ) then
5:        $\mathcal{L}_{IG} = \mathcal{L}_R(f_R(x_t; \theta), y_t)$ 
6:        $\theta \leftarrow \theta + \lambda \nabla (\mathcal{L}_{dt}(f_{dt}(f_R(x_t; \theta)), z_t) + \mathcal{L}_{IG})$ 
7:     else
8:        $\theta \leftarrow \theta + \lambda \nabla (\mathcal{L}_{dt}(f_{dt}(f_R(x_t; \theta)), z_t))$ 
9:     end if
10:     $D'_t \leftarrow x_t, f_R(x_t; \theta), f_{dt}(f_R(x_t; \theta))$ 
11:    if modular( $k, K$ ) == 0 then
12:       $x', y', z' \leftarrow \mathcal{M}$ 
13:       $\mathcal{L}_{IG} = \mathcal{L}_R(f_R(x'; \theta), y')$ 
14:       $\theta \leftarrow \theta + \lambda \nabla (\mathcal{L}_{dt}(f_{dt}(f_R(x'; \theta)), z') + \mathcal{L}_{IG})$ 
15:    end if
16:  end for
17:   $\mathcal{M} \leftarrow \text{Reservoir}(\mathcal{M}, \text{Sample}(D'_t))$ 
18: end for

```

performance of the reconstruction network:

$$\mathcal{L}_{IG} = \mathcal{L}_R(f_R(x_t; \theta), y_t). \quad (5)$$

The reconstructed image is saved to the buffer to compute the loss for past tasks. The overall pipeline of MOST is summarized in Algorithm 1.

IV. EXPERIMENTS AND RESULTS

A. Dataset

T_1 -weighted images from the five distinct datasets of the five tasks were utilized: FastMRI [12], OASIS-1 [44], BraTS [45], IXI [46], and ADNI [47] for image reconstruction, white matter (WM) segmentation, tumor segmentation, sex classification, and Alzheimer's disease (AD) classification tasks, respectively. We excluded images with large artifacts or images without labels. All images were resized as summarized in Table 1 and normalized by the 99th percentile intensity value of the whole brain. To simulate undersampled k-space data, a forward model was applied to the fully sampled data, assuming a single-coil scenario [12] with an acceleration factor of four and a central k-space fraction of 0.08. The WM segmentation utilized the tissue segmentation maps in the OASIS 1 dataset, exclusively selecting the WM region. For the tumor segmentation, all regions except the tumor or edema were labeled as non-tumor. The labels for sex and AD were from the datasets. The mild cognitive impairment cohort in ADNI was omitted from the dataset. Each task dataset was bifurcated into two segments: one designated for the initial pretraining of the downstream task, and the other for the subsequent finetuning procedure. Table I summarizes the details of the datasets.

B. Training details

The neural network part of the variational network was designed by a U-net architecture [48] comprising four downsampling and four upsampling blocks. Each block consists of a repeated sequence of a convolution layer, instance normalization, and leaky-ReLU activation function.

TABLE II

THE LAST METRIC AND FORGETTING MEASURE OF SSIM FOR THE RECONSTRUCTION, DICE FOR THE SEGMENTATION, AND AUC FOR THE CLASSIFICATION ARE REPORTED IN THE TABLE. MOST CONSISTENTLY DEMONSTRATED FAVORABLE PERFORMANCES.

	Recon SSIM	WM seg DICE	Tumor seg DICE	Sex class AUC	AD class AUC
Last metric (\uparrow)					
Recon Label Input	-	0.976	0.685	0.983	0.810
Without Finetuning	0.977	0.861	0.564	0.983	0.800
Naïve Finetuning	0.866	0.835	0.445	0.976	0.812
MOST (ours)	0.971	0.938	0.642	0.983	0.813
Forgetting measure (\downarrow)					
Naïve Finetuning	0.110	0.098	0.179	0.007	-
MOST (ours)	0.006	0.002	0.003	0.000	-

TABLE III
RESULT OF LAST METRIC (LM) AND FORGETTING MEASURES (FM) WITH THREE DIFFERENT DOWNSTREAM TASK ORDERS ARE ILLUSTRATED.

	Reconstruction		WM segmentation		Tumor segmentation		Sex classification		AD classification	
	SSIM	DICE	SSIM	DICE	SSIM	DICE	AUC	AUC	AUC	AUC
Without Finetuning	LM (↑) 0.977	FM (↓) -	LM (↑) 0.861	FM (↓) -	LM (↑) 0.564	FM (↓) -	LM (↑) 0.983	FM (↓) -	LM (↑) 0.800	FM (↓) -
Order 1: Reconstruction → WM segmentation → Tumor segmentation → Sex classification → AD classification										
Naïve Finetuning MOST (ours)	0.866 0.971	0.110 0.006	0.835 0.938	0.098 0.002	0.445 0.642	0.179 0.003	0.976 0.983	0.007 0.000	0.812 0.813	-
Order 2: Reconstruction → Tumor segmentation → AD classification → WM segmentation → Sex classification										
Naïve Finetuning MOST (ours)	0.843 0.970	0.133 0.007	0.930 0.936	0.002 0.001	0.453 0.641	0.181 0.010	0.977 0.983	- -	0.761 0.804	0.051 0.012
Order 3: Reconstruction → Sex classification → AD classification → Tumor segmentation → WM segmentation										
Naïve Finetuning MOST (ours)	0.791 0.959	0.186 0.018	0.934 0.920	- -	0.421 0.598	0.207 0.037	0.956 0.983	0.031 0.000	0.761 0.802	0.053 0.007

Downsampling is achieved through average pooling, while upsampling is performed using transposed convolutions. Additionally, the architecture features skip connections to preserve spatial information across layers. Training proceeded for 50 epochs utilizing the SSIM loss as the loss function. Optimization was carried out using the Adam optimizer with a learning rate of 0.001.

We also employed the same U-net architecture for the segmentation tasks. The network was trained over 50 epochs using a cross-entropy loss function, optimized with the Adam optimizer at a learning rate of 0.001.

The classification task is facilitated by a CNN architecture. It consists of five blocks, each containing a 3D convolutional layer, batch normalization, ReLU activation, and max pooling. Following the convolutional layers, the resultant features are flattened into a one-dimensional vector. This is then fed into two fully connected layers with ReLU activation. The final

layer, also fully connected, yields the classification output. Training proceeded for 70 epochs, employing cross entropy as the loss function. Optimization was conducted using the Adam optimizer, with an initial learning rate set to 0.0001.

The finetuning process for each downstream task was conducted for 5 epochs, and the network with the minimum validation loss was chosen. For the classification tasks, individual slices of a 3D volume were processed through the reconstruction network and then the reconstructed 3D volume was inputted to the classification network. We utilized buffer data every three iterations (K=3).

C. Performance evaluation

We compared the performance of our MOST approach with a reconstruction network without downstream task-oriented finetuning (Without Finetuning) and a reconstruction network with naïve sequential finetuning (Naïve Finetuning). Additionally, performance when the aliasing-free image was inputted to the downstream task network was calculated (Recon Label Input). The buffer size was fixed to 10 subjects (see section IV.F for the buffer size test). The order of the tasks was white matter (WM) segmentation, tumor segmentation, sex classification, and finally Alzheimer's disease (AD) classification (see Section IV.D for the downstream task order test).

We assessed the quality of the reconstructed images using the structural similarity index (SSIM), segmentation results with the Dice similarity coefficient (DICE), and classification performance with the area under the curve (AUC) after completing finetuning for the last downstream task (Last Metric; LM). Additionally, forgetting measures (FM) were computed to quantify how much a model forgot previously learned tasks as it learned new ones. The forgetting measures were calculated by the difference between the best metric and the worst metric of a task obtained during sequential finetuning.

The qualitative results of the reconstruction and WM segmentation tasks are illustrated in Fig. 3. Without task-oriented finetuning (Fig. 3, third column), the reconstructed images demonstrate good reconstruction quality for the reconstruction dataset, but they exhibit subpar reconstructed images and segmentation results due to domain gaps or error propagation for the WM segmentation dataset. On the other hand, Naïve Finetuning results in poor quality in both reconstruction and segmentation, indicating catastrophic forgetting (Fig. 3, fourth column). Finally, the MOST approach

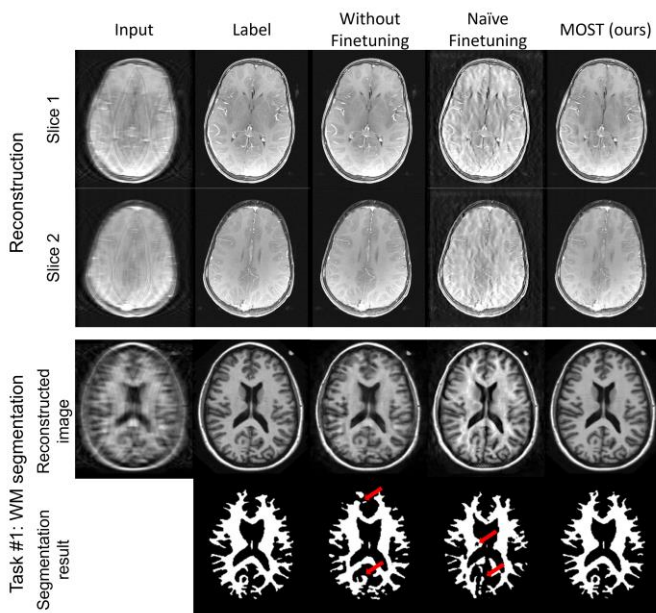


Fig. 3 The results of the reconstruction and WM segmentation before and after the task-specific finetuning are illustrated. Without finetuning, the reconstructed images demonstrate good reconstruction quality but exhibit subpar segmentation results (second column). Naïve finetuning shows poor quality in both reconstruction and segmentation, indicating catastrophic forgetting (third column). MOST effectively mitigates this issue, ensuring high-quality results in both reconstruction and segmentation (last column).

TABLE IV

COMPARISON RESULT OF LAST METRIC (LM) AND FORGETTING MEASURES (FM) TO THE OTHER CONTINUAL LEARNING METHODS ARE ILLUSTRATED.

	Reconstruction		WM segmentation		Tumor segmentation		Sex classification		AD classification	
	SSIM	DICE	SSIM	DICE	SSIM	DICE	AUC	AUC	AUC	AUC
	LM (\uparrow)	FM (\downarrow)	LM (\uparrow)	FM (\downarrow)	LM (\uparrow)	FM (\downarrow)	LM (\uparrow)	FM (\downarrow)	LM (\uparrow)	FM (\downarrow)
Naïve Finetuning	0.866	0.110	0.835	0.098	0.445	0.179	0.976	0.007	0.812	-
EWC [20]	0.910	0.066	0.884	0.048	0.536	0.085	0.976	0.007	0.808	-
LWF [21]	0.937	0.040	0.892	0.026	0.488	0.057	0.893	0.041	0.785	-
ER [30]	0.953	0.024	0.859	0.073	0.479	0.154	0.965	0.018	0.810	-
DER [27]	0.971	0.006	0.929	0.004	0.622	0.000	0.981	0.002	0.809	-
MOST (ours)	0.971	0.006	0.938	0.002	0.642	0.003	0.983	0.000	0.813	

effectively mitigates this issue, producing high-quality results in both reconstruction and WM segmentation tasks (Fig. 3, last column).

Table II provides the quantitative metrics after training the last tasks and the corresponding forgetting measures. When compared to the Without Finetuning, MOST successfully improved performance in all four downstream tasks while slightly sacrificing reconstruction quality, demonstrating that the downstream task-oriented finetuning process helps to increase the performance of the downstream tasks (e.g., Reconstruction SSIM: 0.977 \rightarrow 0.971, WM segmentation DICE: 0.861 \rightarrow 0.938, AD classification AUC: 0.800 \rightarrow 0.813). When compared to the Naïve Finetuning case, MOST exhibited superior LM and FM, demonstrating its effectiveness in preventing catastrophic forgetting and sustaining performance. For example, in WM segmentation, MOST showed an LM of 0.938 and FM of 0.002, which are superior to the LM (0.835) and FM (0.098) of Naïve Finetune. Moreover, it can be observed that the metric of MOST is comparable to the Recon Label Input case, which presumably produces the best outcome (see the second and fifth rows in Table II).

D. Task order test

Task order experiments were conducted with three different downstream task orders: WM segmentation, tumor segmentation, sex classification, and AD classification (Order 1; default); tumor segmentation, AD classification, WM segmentation, and sex classification (Order 2); and sex classification, AD classification, tumor segmentation, and WM segmentation (Order 3). For the three different task orders, we compared the performance of the MOST approach with the Without Finetuning and Naïve Finetuning cases (Table III). When compared to Without Finetuning and Naïve Finetuning, MOST exhibited superior LM and FM in most of the tasks and task orders, demonstrating little dependency on the task order (best scores are in BOLD). When compared across the orders, starting with segmentation proved slightly beneficial in improving the performance, as indicated by an inferior LM and FM in Order 3 when compared to Orders 1 and 2.

E. Comparison with other continual learning methods

We also compared the results to conventional continual learning methods including Elastic Weight Consolidation (EWC) [22], Learning Without Forgetting (LWF) [23], a memory-based method (ER) [26], and another replay-based method (DER) [27].

In employing EWC [22], we adhered to the original methodology, utilizing the Fisher information matrix by

computing the squared gradient of the loss from the preceding task, which then served as a regularization term for the network parameters with λ set to 15. In the implementation of LWF [23], we utilized the last iteration block of the reconstruction network as the dynamic component of the method. The knowledge distillation loss was computed using SSIM to evaluate the discrepancy between the current and previous outputs, setting the regularization coefficient to 1. Rehearsal strategies were also integrated, mirroring our approach of routinely incorporating data from previous tasks. ER [26] incorporated input-label pairs from prior tasks, whereas DER [27] leveraged input-output pairs. The buffer size of rehearsal strategies was fixed to 10 subjects.

The performance comparison results among the continual learning methods, as detailed in Table IV, clearly demonstrated that the MOST approach achieved overall superior performance compared to the other continual learning methods. In contrast, EWC, LWF, ER, and DER showed varying degrees of forgetting and performance degradation. These findings emphasized the advantages of MOST over the conventional continual learning methods, mostly coming from the fact that the image-guided loss can give richer information.

F. Buffer size test

When three different buffer sizes (4, 10, and 50 subjects) were evaluated, the results reported consistent performances as shown in Table V, indicating that MOST performed well even with the buffer size of 4. The unit for the buffer size was in the number of subjects.

TABLE V
MOST WITH VARIOUS BUFFER SIZES IS TESTED. MOST SHOWED STABLE PERFORMANCE FOR DIFFERENT BUFFER SIZES.

Buffer size (Subjects)	Recon SSIM	WM seg DICE	Tumor seg DICE	Sex class AUC	AD class AUC
Last metric (\uparrow)					
4	0.970	0.933	0.640	0.982	0.810
10	0.971	0.938	0.642	0.983	0.813
50	0.970	0.937	0.640	0.981	0.810
Forgetting measure (\downarrow)					
4	0.007	0.007	0.006	0.001	-
10	0.006	0.002	0.003	0.000	-
50	0.007	0.003	0.004	0.003	-

G. Ablation study

To assess the independent contributions of replay-based continual learning and image-guided loss to the performance of MOST, an ablation study was conducted. Three networks were compared: original MOST, MOST without replay-based continual learning, and MOST without image-guided loss. MOST without replay-based continual learning excluded the

TABLE VI
ABLATION STUDY WITHOUT REPLAY-BASED CONTINUAL LEARNING
AND/OR IMAGE-GUIDED LOSS IS ILLUSTRATED.

Replay-based continual learning	Image guided loss	Recon SSIM	WM seg DICE	Tumor seg DICE	Sex class AUC	AD class AUC
Last metric (\uparrow)						
X	O	0.950	0.883	0.604	0.976	0.817
O	X	0.971	0.929	0.622	0.981	0.809
O	O	0.971	0.938	0.642	0.983	0.813
Forgetting measure (\downarrow)						
X	O	0.026	0.056	0.046	0.007	-
O	X	0.006	0.004	0.000	0.002	-
O	O	0.006	0.002	0.003	0.000	-

buffer while retaining the image-guided loss and utilized a combined loss function (task loss + image-guided loss) for downstream task-oriented finetuning. MOST without image-guided loss solely relied on the task loss function for finetuning, while maintaining the buffer.

Table VI presents the results of the ablation study. The ablation study results demonstrated that original MOST largely outperformed MOST without either replay-based continual learning or image-guided loss.

H. Reconstruction network test

A comparison of two different reconstruction networks, a variational network and U-net, was conducted. To measure the effect of network structure in preventing catastrophic forgetting, naïve finetuning was performed with the reconstruction networks for the sequence of downstream tasks with Order 1. Table VII provides a comprehensive comparison between the variational network and U-net. The table clearly demonstrates that the variational network outperforms U-net across all tasks in terms of the metric after the last task finetuning.

V. DISCUSSION

In this work, we demonstrated that a single reconstruction network can be sequentially finetuned for multiple downstream tasks by deploying continual learning. This outcome successfully generalized recently illustrated single downstream task-oriented reconstruction optimization to multiple downstream tasks. In particular, the application of replay-based continual learning along with the newly proposed image-guided loss successfully prevented catastrophic forgetting, which was observed in naïve finetuning.

Reconstruction network performance has recently been evaluated by measuring the performance of a downstream task network (e.g., segmentation network) on the reconstructed images. This downstream task-oriented evaluation offers a distinct advantage over traditional image-level evaluation metrics such as PSNR and SSIM because visually appealing images may not translate into the input requirement of a downstream task as demonstrated in the previous studies [16–19]. In this work, we extended this idea for multiple downstream tasks. This setup better aligns with current clinical practice where multiple neural networks of different tasks are progressively developed and applied.

In our study, MOST showed overall performance improvement in all task orders when compared to that of Naïve

Finetuning, but it did show task order dependency (Table III). In particular, MOST fell short in Order 3, which may be attributed to the introduction of classification tasks earlier than segmentation tasks. Classification labels had less information than segmentation labels, leading to less effective finetuning.

Our proposed framework is based on the single-coil setting, wherein the reconstruction model takes single k-space data as the input and produces an alias-free image as the output. The reason for the single-coil setting is limited available end-to-end datasets that include multi-coil k-space data and classification/segmentation labels. The adaptation of this framework to multi-coil data may require conversion to the multi-coil variational network that includes coil sensitivity estimation.

Current continual learning methods mostly target high-level computer vision tasks like classification or segmentation, [49] because catastrophic forgetting rarely arises in regression tasks. In our scenario, although we employ sequential training for the regression network, the cascaded network ultimately performs classifications or segmentations. Hence catastrophic forgetting occurs in the downstream tasks. If the reconstruction network is merely finetuned with the original reconstruction task for different domains (e.g., images with different scanners or different parameters), the effect of catastrophic forgetting may decrease, and continual learning methodologies may not be required.

Beyond replay-based continual learning or image-guided losses, the reconstruction network itself offers advantages in mitigating catastrophic forgetting. We leverage a variational network [16] as the reconstruction network. Enforcing the forward model within this network minimizes output variability, thereby alleviating catastrophic forgetting. (Table VII)

In our approach, we manually trained the downstream task networks instead of adopting off-the-shelf state-of-the-art (SOTA) models. This resulted in inferior metrics compared to those from SOTA models. This manual training was utilized because the off-the-shelf SOTA model is trained on the entire training dataset of the model. On the other hand, we required the training dataset to be split into the downstream network training part and the reconstruction network finetuning part. Moreover, the BraTS dataset contained multimodal MRI data with T_1 -weighted, T_2 -weighted, and contrast agent-enhanced images, but we only used the T_1 -weighted images to maintain consistency with other tasks. Additionally, most SOTA models included preprocessing steps on the input image, such as skull stripping or registration to a template. Incorporating these preprocessing steps in MOST is not straightforward and therefore requires further investigation.

VI. CONCLUSION

In this study, we propose a scenario where a reconstruction network is sequentially optimized for multiple downstream tasks and demonstrate that replay-based continual learning techniques can prevent catastrophic forgetting. Through this approach, we effectively address the challenge of catastrophic

TABLE VII
TABLE SHOWS THE COMPARISON OF THE LAST METRIC (LM) AND FORGETTING MEASURE (FM) OF VARIATIONAL NETWORK AND U-NET.

	Reconstruction		WM segmentation		Tumor segmentation		Sex classification		AD classification	
	SSIM	DICE	DICE	DICE	AUC	AUC	LM (↑)	FM (↓)	LM (↑)	FM (↓)
Variational network	0.866	0.110	0.835	0.098	0.445	0.179	0.976	0.007	0.812	-
U-net	0.660	0.282	0.848	0.050	0.437	0.134	0.973	0.006	0.786	

forgetting in multiple downstream tasks, paving the way for the development of a more robust and versatile MR reconstruction network in a realistic clinical setup.

APPENDIX

Variational network Variational networks leveraged the advantages of both model-based and learning-based methodologies by integrating a physical forward model of MRI acquisition with deep learning technique, resulting in state-of-the-art performance in MRI reconstruction. Traditionally, the problem of single-coil MR reconstruction is formulated as follows:

$$\hat{x} = \operatorname{argmin}_x \frac{1}{2} \|M\mathcal{F}x - \hat{k}\|^2 + \lambda\Phi(x), \quad (\text{A1})$$

where \hat{x} is resultant reconstructed image, M is undersampling mask, \mathcal{F} is 2D Fourier Transform, \hat{k} is the undersampled k-space data, and Φ is a regularization function. We set $A = M\mathcal{F}$. Solving this problem typically involves an iterative gradient descent method, where in the n -th step, the image is updated from x^n to x^{n+1} using the following update rule:

$$x^{n+1} = x^n - \eta^n \left(A^*(Ax^n - \hat{k}) + \lambda\nabla\Phi(x^n) \right), \quad (\text{A2})$$

where η^n is the learning rate, and A^* is the Hermitian of the matrix A . The regularization function in (A1) is replaced by a convolutional neural network [10],[61]:

$$x^{n+1} = x^n - \eta^n A^*(Ax^n - \hat{k}) + CNN(x^n), \quad (\text{A3})$$

Training is conducted in an end-to-end manner, where the loss function is computed between the aliasing-free image y and the output of the last iteration x^N .

REFERENCES

- [1] H.-I. Suk, S.-W. Lee, D. Shen *et al.*, “Hierarchical feature representation and multimodal fusion with deep learning for AD/MCI diagnosis,” *NeuroImage*, vol. 101, pp. 569-582, 2014.
- [2] F. Li, L. Tran, K.-H. Thung *et al.*, “A robust deep model for improved classification of AD/MCI patients,” *IEEE J. Biomed. Health Inform.*, vol. 19, no. 5, pp. 1610-1616, 2015.
- [3] R. Cuingnet, E. Gerardin, J. Tessieras *et al.*, “Automatic classification of patients with Alzheimer’s disease from structural MRI: a comparison of ten methods using the ADNI database,” *NeuroImage*, vol. 56, no. 2, pp. 766-781, 2011.
- [4] Y. Noh, Y. Sung, J. Lee *et al.*, “Nigrosome 1 detection at 3T MRI for the diagnosis of early-stage idiopathic Parkinson disease: assessment of diagnostic accuracy and agreement on imaging asymmetry and clinical laterality,” *Am. J. Neuroradiol.*, vol. 36, no. 11, pp. 2010-2016, 2015.
- [5] L. Chen, P. Bentley, and D. Rueckert, “Fully automatic acute ischemic lesion segmentation in DWI using convolutional neural networks,” *Neuroimage Clin.*, vol. 15, pp. 633-643, 2017.
- [6] M. Hawaie, A. Davy, D. Warde-Farley *et al.*, “Brain tumor segmentation with deep neural networks,” *Med. Image Anal.*, vol. 35, pp. 18-31, 2017.
- [7] D. Shin, S. Ji, D. Lee *et al.*, “Deep Reinforcement Learning Designed Shinnar-Le Roux RF Pulse Using Root-Flipping: DeepRF SLR,” *IEEE Trans. Med. Imaging*, vol. 39, no. 12, pp. 4391-4400, 2020.
- [8] J. Yoon, E. Gong, I. Chatnuntawech *et al.*, “Quantitative susceptibility mapping using deep neural network: QSMnet,” *Neuroimage*, vol. 179, pp. 199-206, 2018.
- [9] J. Lee, D. Lee, J. Y. Choi *et al.*, “Artificial neural network for myelin water imaging,” *Magn. Reson. Med.*, vol. 83, no. 5, pp. 1875-1883, 2020.
- [10] K. Hammernik, T. Klatzer, E. Kobler *et al.*, “Learning a variational network for reconstruction of accelerated MRI data,” *Magn. Reson. Med.*, vol. 79, no. 6, pp. 3055-3071, 2018.
- [11] H. K. Aggarwal, M. P. Mani, and M. Jacob, “MoDL: Model-based deep learning architecture for inverse problems,” *IEEE Trans. Med. Imaging*, vol. 38, no. 2, pp. 394-405, 2018.
- [12] J. Zbontar, F. Knoll, A. Sriram *et al.*, “fastMRI: An open dataset and benchmarks for accelerated MRI,” *arXiv preprint arXiv:1811.08839*, 2018.
- [13] M. J. Muckley, B. Riemenschneider, A. Radmanesh *et al.*, “Results of the 2020 fastMRI challenge for machine learning MR image reconstruction,” *IEEE Trans. Med. Imaging*, vol. 40, no. 9, pp. 2306-2317, 2021.
- [14] A. D. Desai, A. M. Schmidt, E. B. Rubin *et al.*, “Skm-tea: A dataset for accelerated mri reconstruction with dense image labels for quantitative clinical evaluation,” *arXiv preprint arXiv:2203.06823*, 2022.
- [15] A. D. Desai, F. Caliva, C. Iriondo *et al.*, “The international workshop on osteoarthritis imaging knee MRI segmentation challenge: a multi-institute evaluation and analysis framework on a standardized dataset,” *Radiol.: Artif. Intell.*, vol. 3, no. 3, pp. e200078, 2021.
- [16] Z. Fan, L. Sun, X. Ding *et al.*, “A segmentation-aware deep fusion network for compressed sensing mri,” in Proc. European Conf. Comput. Vis (ECCV), 2018, pp. 55-70.
- [17] L. Sun, Z. Fan, X. Ding *et al.*, “Joint CS-MRI reconstruction and segmentation with a unified deep network,” in Proc. Inf. Process. Med. Imaging (IPMI), 2019, pp. 492-504.
- [18] Z. Wang, W. Xia, Z. Lu *et al.*, “One network to solve them all: A sequential multi-task joint learning network framework for MR imaging pipeline,” in Proc. Int. Workshop Mach. Learn. Med. Image Reconstruction (MLMIR), 2021, pp. 76-85.
- [19] Z. Wu, T. Yin, Y. Sun *et al.*, “Learning Task-Specific Strategies for Accelerated MRI,” *arXiv preprint arXiv:2304.12507*, 2023.
- [20] O. Sener, and V. Koltun, “Multi-task learning as multi-objective optimization,” *Adv. Neural Inf. Process. Syst.*, vol. 31, 2018.
- [21] R. Aljundi, F. Babiloni, M. Elhoseiny *et al.*, “Memory aware synapses: Learning what (not) to forget,” in Proc. European Conf. Comput. Vis (ECCV), 2018, pp. 139-154.
- [22] J. Kirkpatrick, R. Pascanu, N. Rabinowitz *et al.*, “Overcoming catastrophic forgetting in neural networks,” *Proc. Natl. Acad. Sci. U.S.A.*, vol. 114, no. 13, pp. 3521-3526, 2017.
- [23] Z. Li, and D. Hoiem, “Learning without forgetting,” *IEEE Trans. Pattern Anal. Mach. Intell.*, vol. 40, no. 12, pp. 2935-2947, 2017.
- [24] X. Li, Y. Zhou, T. Wu *et al.*, “Learn to grow: A continual structure learning framework for overcoming catastrophic forgetting,” in Proc. Int. Conf. Mach. Learn. (ICML), 2019, pp. 3925-3934.
- [25] N. Loo, S. Swaroop, and R. E. Turner, “Generalized variational continual learning,” *arXiv preprint arXiv:2011.12328*, 2020.

[26] A. Chaudhry, M. Rohrbach, M. Elhoseiny *et al.*, “On tiny episodic memories in continual learning,” *arXiv preprint arXiv:1902.10486*, 2019.

[27] P. Buzzega, M. Boschini, A. Porrello *et al.*, “Dark experience for general continual learning: a strong, simple baseline,” *Adv. Neural Inf. Process. Syst.*, vol. 33, pp. 15920-15930, 2020.

[28] Y. Chen, C.-B. Schönlieb, P. Liò *et al.*, “AI-based reconstruction for fast MRI—a systematic review and meta-analysis,” *Proc. IEEE*, vol. 110, no. 2, pp. 224-245, 2022.

[29] J. Schlemper, J. Caballero, J. V. Hajnal *et al.*, “A deep cascade of convolutional neural networks for MR image reconstruction,” in *Proc. Inf. Process. Med. Imaging (IPMI)*, 2017, pp. 647-658.

[30] C. M. Hyun, H. P. Kim, S. M. Lee *et al.*, “Deep learning for undersampled MRI reconstruction,” *Phys. Med. Biol.*, vol. 63, no. 13, pp. 135007, 2018.

[31] B. Zhu, J. Z. Liu, S. F. Cauley *et al.*, “Image reconstruction by domain-transform manifold learning,” *Nature*, vol. 555, no. 7697, pp. 487-492, 2018.

[32] M. A. Mazurowski, M. Buda, A. Saha *et al.*, “Deep learning in radiology: An overview of the concepts and a survey of the state of the art with focus on MRI,” *J. Magn. Reson. Imaging*, vol. 49, no. 4, pp. 939-954, 2019.

[33] N. Garg, M. S. Choudhry, and R. M. Bodade, “A review on Alzheimer’s disease classification from normal controls and mild cognitive impairment using structural MR images,” *J. Neurosci. Methods*, vol. 384, pp. 109745, 2023.

[34] W. H. L. Pinaya, A. Gadelha, O. M. Doyle *et al.*, “Using deep belief network modelling to characterize differences in brain morphometry in schizophrenia,” *Sci. Rep.*, vol. 6, no. 1, pp. 38897, 2016.

[35] N. Abiwinanda, M. Hanif, S. T. Hesaputra *et al.*, “Brain tumor classification using convolutional neural network,” in *World Congress on Medical Physics and Biomedical Engineering*, 2019, pp. 183-189.

[36] O. Commowick, F. Cervenansky, and R. Ameli, “MSSEG challenge proceedings: multiple sclerosis lesions segmentation challenge using a data management and processing infrastructure,” in *Proc. Int. Conf. Med. Image Comput. Comput.-Assist. Intervent (MICCAI)*, 2016.

[37] A. M. Mendrik, K. L. Vincken, H. J. Kuijf *et al.*, “MRBrainS challenge: online evaluation framework for brain image segmentation in 3T MRI scans,” *Comput. Intell. Neurosci.*, vol. 2015, pp. 1-1, 2015.

[38] Q. Dou, H. Chen, L. Yu *et al.*, “Automatic cerebral microbleeds detection from MR images via independent subspace analysis based hierarchical features,” in *Proc. Annu. Int. Conf. IEEE Eng. Med. Biol. Soc. (EMBC)*, 2015, pp. 7933-7936.

[39] M. Perkonigg, J. Hofmanninger, C. J. Herold *et al.*, “Dynamic memory to alleviate catastrophic forgetting in continual learning with medical imaging,” *Nat. Commun*, vol. 12, no. 1, pp. 5678, 2021.

[40] S. Özgün, A.-M. Rickmann, A. G. Roy *et al.*, “Importance driven continual learning for segmentation across domains,” in *Proc. Int. Workshop Mach. Learn. Med. Imag. (MLMI)*, 2020, pp. 423-433.

[41] C. Baweja, B. Glocker, and K. Kamnitsas, “Towards continual learning in medical imaging,” *arXiv preprint arXiv:1811.02496*, 2018.

[42] A. Prabhu, P. H. S. Torr, and P. K. Dokania, “Gdumb: A simple approach that questions our progress in continual learning,” in *Proc. European Conf. Comput. Vis. (ECCV)*, 2020.

[43] H. Cha, J. Lee, and J. Shin, “Co2L: Contrastive continual learning,” in *Proc. IEEE Int. Conf. Comput. Vis. (ICCV)*, 2021, pp. 9516-9525.

[44] D. S. Marcus, T. H. Wang, J. Parker *et al.*, “Open Access Series of Imaging Studies (OASIS): cross-sectional MRI data in young, middle aged, nondemented, and demented older adults,” *J. Cogn. Neurosci.*, vol. 19, no. 9, pp. 1498-1507, 2007.

[45] B. H. Menze, A. Jakab, S. Bauer *et al.*, “The multimodal brain tumor image segmentation benchmark (BRATS),” *IEEE Trans. Med. Imaging*, vol. 34, no. 10, pp. 1993-2024, 2014.

[46] “IXI - Information eXtraction from Images.”

[47] C. R. Jack Jr, M. A. Bernstein, N. C. Fox *et al.*, “The Alzheimer’s disease neuroimaging initiative (ADNI): MRI methods,” *J. Magn. Reson. Imaging*, vol. 27, no. 4, pp. 685-691, 2008.

[48] O. Ronneberger, P. Fischer, and T. Brox, “U-net: Convolutional networks for biomedical image segmentation,” in *Proc. Int. Conf. Med. Image Comput. Comput.-Assist. Intervent (MICCAI)*, 2015, pp. 234-241.

[49] R. Hadsell, D. Rao, A. A. Rusu *et al.*, “Embracing change: Continual learning in deep neural networks,” *Trends Cognit. Sci.*, vol. 24, no. 12, pp. 1028-1040, 2020.